Measurement 231 (2024) 114592

Contents lists available at ScienceDirect

Measurement

journal homepage: www.elsevier.com/locate/measurement

A cross-polarized antenna sensor based on U-shaped resonator for crack sensing

Kang Jiang [a], Songtao Xue [a,b], Liyu Xie [a,*], Guochun Wan [c]

[a] Department of Disaster Mitigation for Structures, Tongji University, Shanghai, China
[b] Department of Architecture, Tohoku Institute of Technology, Sendai, Japan
[c] Department of Electronic Science and Technology, Tongji University, Shanghai, China

ARTICLE INFO

Keywords:
Antenna sensor
Structural health monitoring
Passive
Wireless
Cross polarization

ABSTRACT

To address the insufficient strain transfer ratio of monolithic antenna sensors and signal self-jamming in wireless interrogation, this paper presents a cross-polarized antenna sensor based on a U-shaped resonator for crack sensing. The sensor comprises an Rx antenna, a Tx antenna, and a sensing element. Employing cross polarization between Rx and Tx antennas mitigates ambient reflection, and the channel model of the sensing system based on cross polarization technique is demonstrated to reveal the working mechanism. Within the sensing element, a U-shaped resonator and movable shorted unit form an unstressed resonator, encoding the crack width in both the amplitude and phase in the retransmission signal, which are utilized to extract the sensor's resonant frequency. The equivalent circuit model is established to analyze the monitoring mechanism comprehensively. The operational performance of the sensor is simulated in CST and validated by experiment. Results demonstrate a good linear relationship between the sensor's resonant frequency and the crack width.

1. Introduction

In civil engineering structures, industrial production, and aerospace, deformation or crack is inevitable due to long-term service or extreme environments, affecting the normal operation and even causing catastrophic accidents [1]. Hence, real-time structural health monitoring (SHM) and comprehensive safety assessment of engineering, civil structures, and industrial electronics are of great significance [2,3].

As an essential component of structural health monitoring, sensors are employed to detect deformation and transmit monitoring data in real-time. Traditional sensors, such as optical fiber sensors [4], resistive transducers [5], and piezoelectric sensors [6], necessitate cables for power supply and transmitting monitoring data. However, the installation of cables increases the system's cost and complexity, making repairs exceedingly inconvenient when the system malfunctions[7]. To avoid the usage of cables, various wireless sensors have been proposed to realize information detection and wireless communication by integrating sensing elements and wireless communication units[8,9]. Nevertheless, these communication devices still require a power supply to ensure uninterrupted operation, which incurs substantial maintenance costs and exhibits diminished performance in high-temperature environments, limiting their practical application. Therefore, passive and wireless sensing systems have been garnering more and more attention lately to achieve continuous, uninterrupted monitoring systems without relying on batteries.

In past decades, Radio Frequency Identification (RFID), an emerging identification technique offering numerous benefits, such as non-line of sight communication path, all-weather reading, low cost, and simplicity, has provided a viable solution for wireless and passive monitoring [10,11]. Among RFID, chipless RFID stands out due to its capability to function without an embedded chip, which further compacts the structure and reduces the tag's cost. Compared with chipped RFID, chipless RFID is suitable for massive deployment [12]. Hence, chipless RFID has recently garnered significant attention in sensor applications. One notable advancement is the antenna sensors, which encode the monitoring information in the electromagnetic characteristic parameters of backscattered signal or retransmitted signal [13]. Meanwhile, the antenna sensor's electromagnetic characteristic parameters are designed to be shifted with structural deformation or changes in environmental parameters. Deif et al. [14] proposed an antenna sensor based on six rectangular spiral resonators for detecting defects in pipeline coating. In the presence of water between the coating and the pipe surface, the resonator at the water-affected area will be short-circuited, resulting in the disappearance of the resonant frequency. Yi et al. [15] utilized a

* Corresponding author.
E-mail address: liyuxie@tongji.edu.cn (L. Xie).

https://doi.org/10.1016/j.measurement.2024.114592
Received 1 December 2023; Received in revised form 17 March 2024; Accepted 25 March 2024
Available online 27 March 2024
0263-2241/© 2024 Elsevier Ltd. All rights reserved.

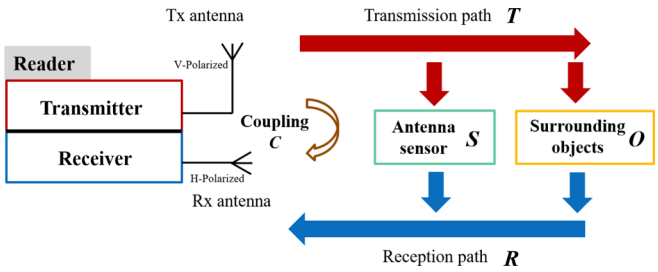

Fig. 1. Channel model of the sensing system.

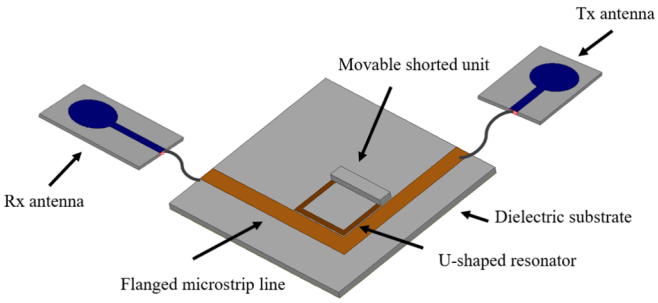

Fig. 2. Schematic of the crack sensor.

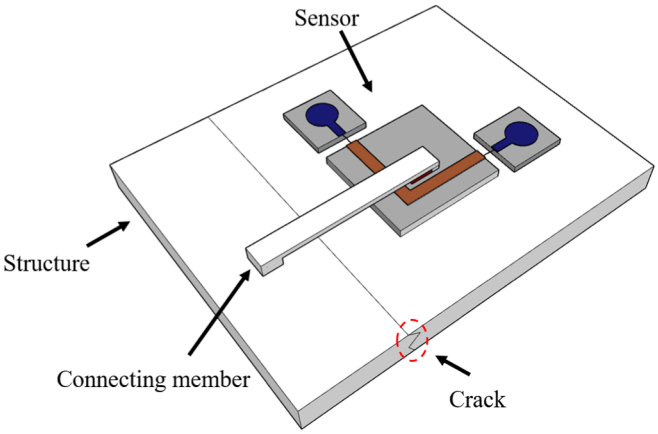

Fig. 3. Installation diagram of the crack sensor.

patch antenna sensor to detect both the setting time and moisture content. With the increase in moisture content, the cement's dielectric constant decreases, consequently increasing the sensor's resonant frequency. Tchafa et al. [16] designed a dual-frequency patch antenna for measuring both the superstrate thickness and temperature simultaneously. Up to now, antenna sensors have shown great application prospects in various fields of SHM [13,17–24].

However, the majority of antenna sensors are based on a monolithic patch antenna to realize the sensing function, facing some the adverse effects of bonding in monitoring structural deformation, such as insufficient strain transfer ratio [25]. Besides, the monolithic antenna sensor utilizes the size alteration of its own patch to detect deformation, which is prone to failure during significant deformations, not conducive to long-term monitoring. To avoid these issues, the combined unstressed antenna sensor has been further studied by scholars, which uses the relative motion of the radiation patch and the sub-patch to characterize the structural deformation, avoiding the stress on the radiation patch [11,26–29]. Zhang et al. [30] introduced a crack sensor comprised of a circular patch antenna and a ground plane related with crack depth. With the increase of crack depth, the effective electrical length of the circular patch will increase, and consequently, the resonant frequency will decrease. Caizzone et al. [31] proposed a crack sensor based on two coupling planar-inverted-F antennas. The change of coupling distance will cause the phase variation of the backscattered field, which is related to crack widths. Xue et al. [32] developed a bolt loosening sensor based on a rectangular patch antenna. The loosening of the bolt will cause the length of the screw to change, consequently altering the overlapped length between the sub-patch and the radiation patch, resulting in a shift in the resonant frequency. Jha et al. [3] designed an angel sensor for detecting rotation and proximity, which utilizes the relative rotation and vertical movement of a complementary split-ring resonator on a conductor-backed coplanar waveguide to change the sensor's resonant frequency.

Although the antenna sensors have attractive prospects in SHM, wireless interrogation in antenna sensors still faces significant challenges. Upon receiving the wireless interrogation signal, the antenna sensor will backscatter signal encoding the detection data outward. Simultaneously, surrounding objects also reflect the interrogation signal. Unfortunately, the intensity of the reflected interrogation signal surpasses that of the backscattered signal, causing the backscattered signal to be submerged in the echo signal, which is the "self-jamming" problem [13]. Several techniques have been developed to separate backscattered signals from echo signals. Among them, the impedance switching technique and the amplitude modulation (AM) technique exhibit similarities, as both necessitate a switch in the sensor node to alter the state of the antenna terminal load for backscattered signal modulation [33,34]. However, the inherent operational requirements of the switch make it reliant on batteries, increasing maintenance costs. Frequency doubling technique aims to elevate the frequency of the backscattered signal to twice the frequency of the interrogation signal, and it is easy to separate the backscattered signal from the environmental reflection signal[20]. Nonetheless, frequency doubling technique entails the use of diodes, increasing the complexity of the sensor. Another approach, background subtraction technique, involves subtracting the echo signal recorded with a sensor from the echo signal obtained without a sensor to isolate the backscattered signal, which means that calibration is required before each interrogation[35]. Cross polarization technique involves adjusting the polarization direction of the backscattered signal to cross the polarization direction of the interrogation signal, while the polarization direction of the reflected signal and interrogation signal is consistent[22,36,37]. Consequently, the reflected signal can easily be filtered out at the receiving terminal of the reader. Compared with the previous several technologies, cross polarization technique utilizes the inherent characteristics of the electromagnetic wave itself, without extra components, thereby offering a simpler operational approach.

This paper introduces a cross-polarized antenna sensor based on a U-shaped resonator for crack sensing. To avoid the high intensity of the ambient reflection signal, the sensor integrates two cross-polarized ultra-wideband (UWB) antennas to receive the interrogation signal and retransmit the encoded signal, which allows the sensor to function properly on metal surfaces. Moreover, a combined unstressed sensing element can encode the crack width in the retransmission signal, avoiding the drawback of forced fracture of the monolithic antenna sensor that affects the service performance and service life. In the sensing element, the shorted unit can be moved above the U-shaped resonator, and there is an overlapped length between the U-shaped resonator and the sub-patch beneath the shorted unit, facilitating current flow from the U-shaped resonator to the sub-patch. Consequently, the sub-patch and U-shaped resonator work together as a combined resonator, causing amplitude attenuation and phase fluctuations to the signal at the resonant frequency. In wireless interrogation, the sensor's resonant frequency can be restored from amplitude and phase simultaneously, enhancing both stability and accuracy. This article is organized as follows. Section 2 reveals the operational mechanism of cross polarization technique and introduces the innovative concept and sensing

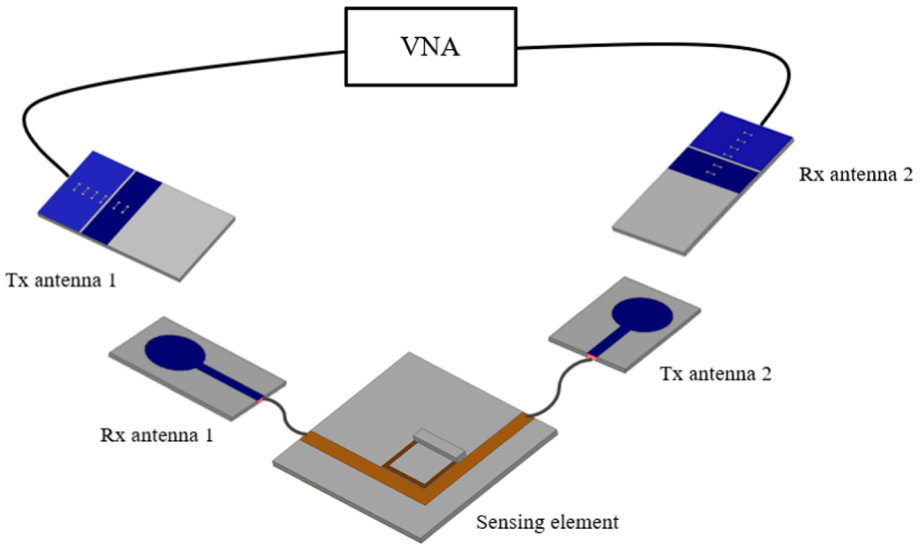

Fig. 4. Wireless interrogation diagram of the sensor.

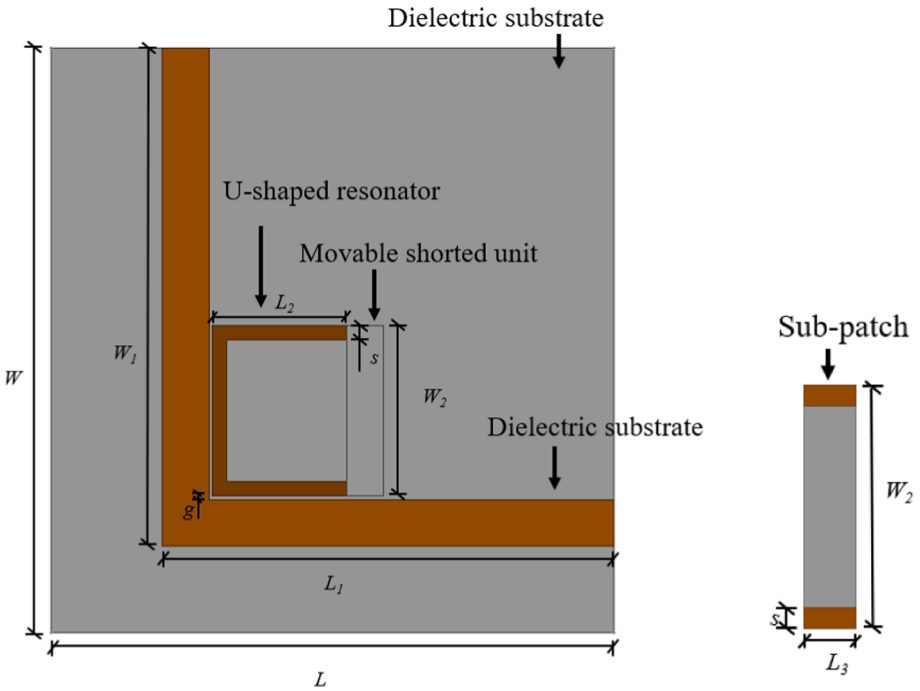

Fig. 5. Dimensional parameters of the sensing unit: (a) Top view of sensing unit and (b) Upward view of movable shorted unit.

principle of the proposed crack sensor. In Section 3, the modeling and simulation of the crack sensor are carried out to study the sensor's resonant frequencies under different crack widths. In Section 4, the sensor is fabricated, and a series of wireless interrogations are conducted to assess the sensor's feasibility. The last section gives the conclusion.

2. Methodology

2.1. Mechanism of cross polarization technique to avoid self-jamming

To elucidate the operational mechanism of cross polarization technique, it is beneficial to establish a channel model of the sensing system, as shown in Fig. 1. The subsequent analysis is primarily based on the literature [38]. The channel model consists of a reader, an antenna sensor and surrounding objects. Furthermore, there is a coupling effect between the transmitting antenna and the receiving antenna of the reader.

Obviously, the signal received by the reader consists of three parts: the antenna sensor's response, the surrounding objects' response and the coupling effect, which can be expressed as:

$$M = T \cdot C \cdot R + T \cdot S \cdot R + T \cdot O \cdot R = I + T \cdot S \cdot R + T \cdot O \cdot R \quad (1)$$

Where M represents the signal received by the reader, T represents the transmission path, R represents the reception path, C represents the coupling effect between the transmitting antenna and the receiving antenna, S represents the response of the antenna sensor, and O represents the response of the surrounding objects. Since the coupling effect is always present, independent of the sensor and the object, it can be represented by a constant matrix I.

Taking into account the polarization of electromagnetic waves, each

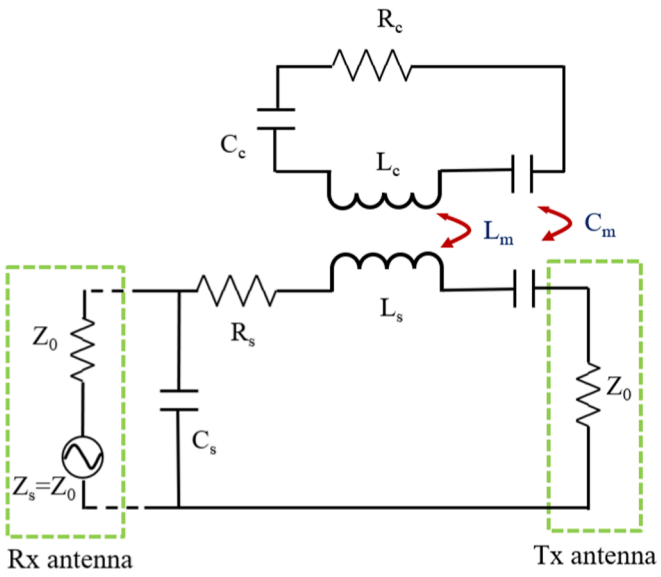

Fig. 6. Equivalent circuit model of the crack sensor.

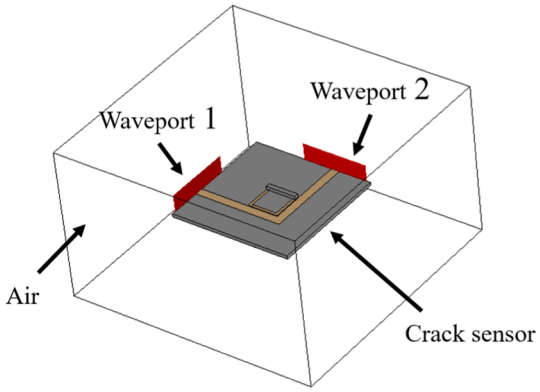

Fig. 7. The model of the crack sensor in CST.

Table 1
Basic Parameters Of the Simulation Settings.

Parameters	Value	Parameters	Value
W / mm	55	L_2 / mm	13
W_1 / mm	40.8	L_3 / mm	2
W_2 / mm	14	s / mm	1.2
L / mm	55	g / mm	0.3
L_1 / mm	40	ΔL / mm	0 ~ 2

block can be expressed as a 2 × 2 scattering matrix. In the scattering matrix, the two terms on the diagonal represent the co-polarization transfer function, while the two others represent the cross-polarization transfer function. The equation (1) can be expressed in more detail as:

$$\begin{bmatrix} M_{vv} & M_{vh} \\ M_{hv} & M_{hh} \end{bmatrix} = \begin{bmatrix} I_{vv} & I_{vh} \\ I_{hv} & I_{hh} \end{bmatrix} + \begin{bmatrix} T_{vv} & T_{vh} \\ T_{hv} & T_{hh} \end{bmatrix} \cdot \left\{ \begin{bmatrix} S_{vv} & S_{vh} \\ S_{hv} & S_{hh} \end{bmatrix} + \begin{bmatrix} O_{vv} & O_{vh} \\ O_{hv} & O_{hh} \end{bmatrix} \right\} \cdot \begin{bmatrix} R_{vv} & R_{vh} \\ R_{hv} & R_{hh} \end{bmatrix} \tag{2}$$

In the sensing system employing cross polarization technique, there is a high degree of isolation between the transmitting and receiving antennas, which means that T_{vh}, T_{hv}, R_{vh}, and R_{vh} are sufficiently low to be negligible. Besides, common objects also do not reflect cross-polarized signals, which means that O_{vh} and O_{hv}, are also low enough to be ignored. Thus, the co-polarized signal received by the reader can

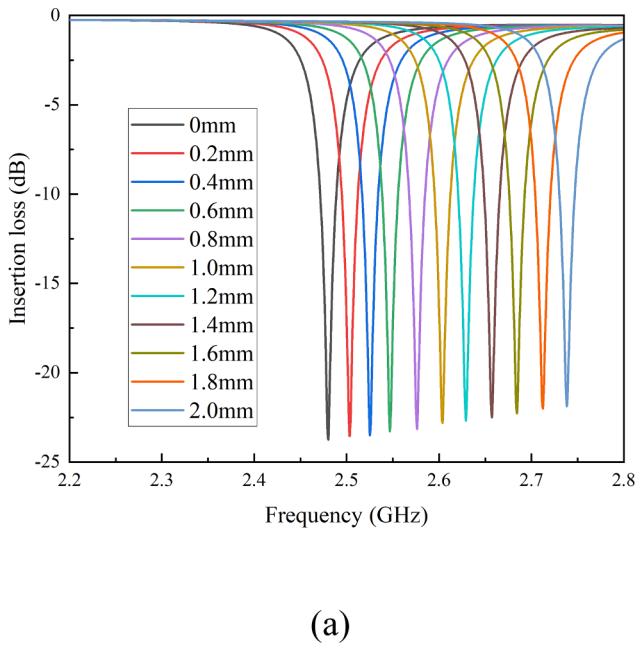

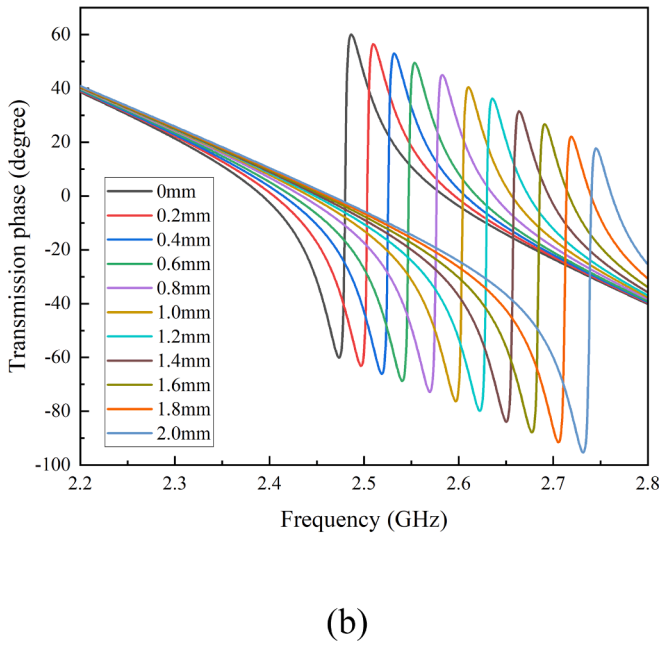

Fig. 8. S21 curve of the crack sensor at different overlapped lengths in CST: (a) insertion loss and (b) transmission phase.

be expressed as:

$$M_{vv} \approx I_{vv} + T_{vv} \cdot (S_{vv} + O_{vv}) \cdot R_{vv} \tag{3}$$

Obviously, increasing the intensity of the transmission signal cannot proportionally enhance the contribution of the sensor response relative to the object in the received signal, which means that useful signals remain buried in ambient reflections.

The cross-polarized signal received by the reader can be expressed as:

$$M_{vh} \approx I_{vh} + T_{vv} \cdot S_{vh} \cdot R_{hh} \tag{4}$$

In contrast to the co-polarized signal, the intensity of the sensor's

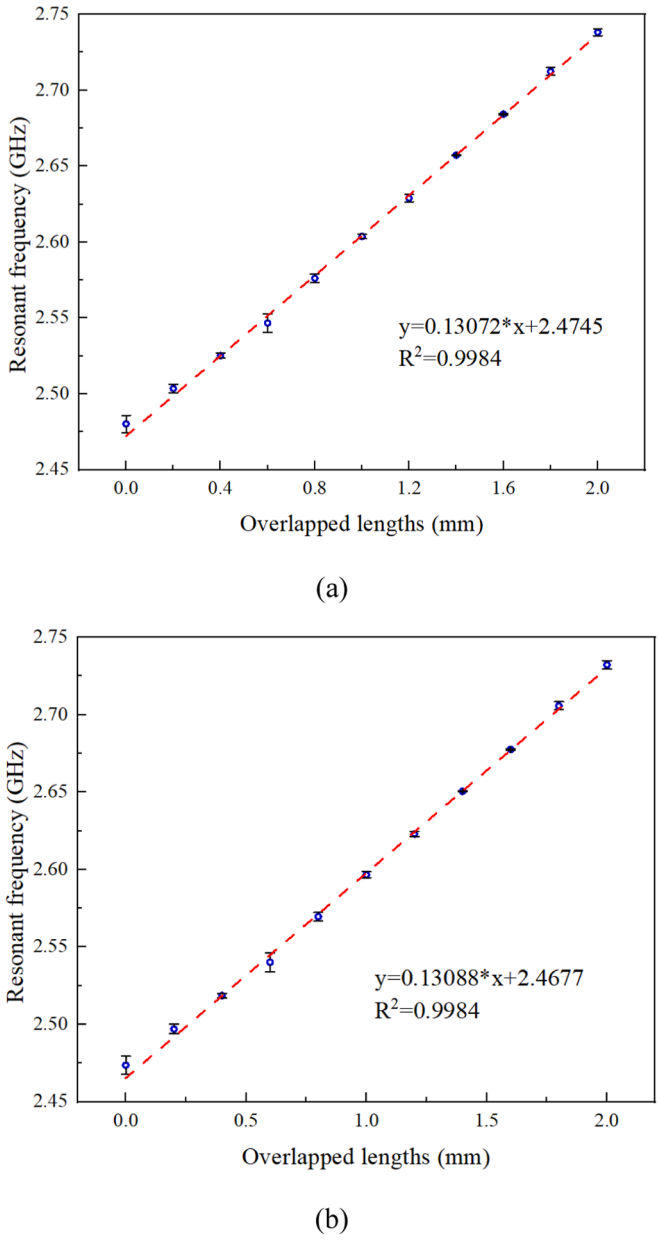

Fig. 9. Relationship between overlapped lengths and resonant frequency in CST calculated from (a) insertion loss and (b) transmission phase.

Table 2
Comparison of calculation methods using insertion loss and transmission phase.

Calculation methods	Lowest point of insertion loss	Initial point of phase fluctuation
Starting frequency (GHz)	2.4802	2.4736
Ending frequency (GHz)	2.7382	2.7322
Fitting factor	0.9984	0.9984
Sensitivity (MHz/mm)	129	129.3

cross-polarized response can be significantly improved by increasing the intensity of the transmission signal, thereby avoiding self-jamming.

2.2. Sensing principle of crack sensor

The crack sensor consists of an Rx antenna, Tx antenna, flanged

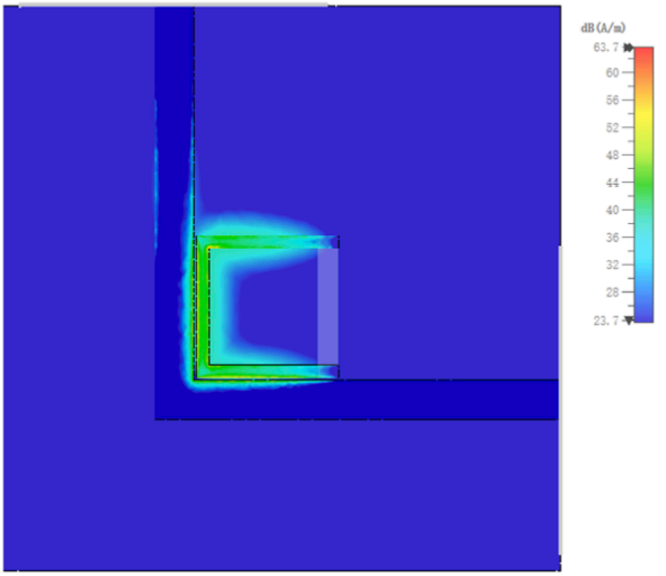

Fig. 10. Current distribution diagram of crack sensor at 2.6 GHz and 1 mm overlapped length.

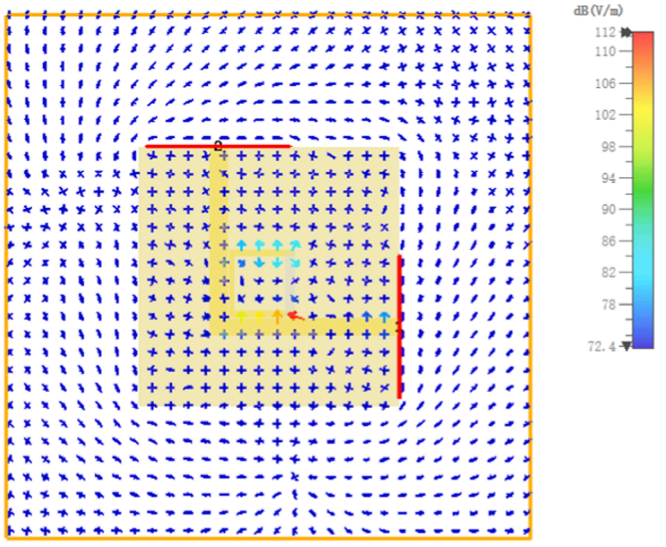

Fig. 11. Electric field distribution diagram of crack sensor at 2.6 GHz and 1 mm overlapped length.

microstrip line, dielectric substrate, ground plane, U-shaped resonator coupled at the flanged corner of the microstrip line, and movable shorted unit, as shown in Fig. 2. Compared with other shapes resonators, such as spiral resonators, U-shaped resonators have a simpler structure and are more suitable for deformation sensing. Meanwhile, the U-shaped resonator is a resonant structure with a high Q-value and narrow bandwidth, which is suitable for wireless sensing. The impedance of the microstrip line is 50 Ohm to reduce transmission losses, and the U-shaped resonator is coupled at the corner of the microstrip line to increase the surface current intensity and energy dissipation at its resonant frequency[39]. The movable shorted unit consists of an overlapping dielectric substrate and an overlapping sub-patch. The movable shorted unit is positioned above the underlying U-shaped resonator. This arrangement ensures a tight fit, with the sub-patch and U-shaped resonator lying in the same plane. The current can flow from the U-shaped resonator to the sub-patch when the sub-patch and U-shaped resonator have a partial overlapped length, which allows the U-shaped resonator

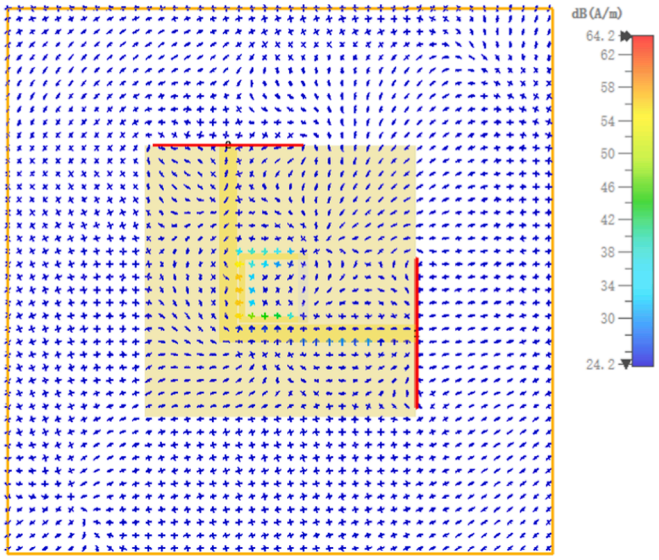

Fig. 12. Magnetic field distribution diagram of crack sensor at 2.6 GHz and 1 mm overlapped length.

and the sub-patch to function collaboratively as a combined resonator to dissipate energy.

In practical applications, the sensor is positioned on one side of the crack, with the shorted unit connected to the opposite side of the crack via a connecting member, as shown in Fig. 3. Initially, the right side of the U-shaped resonator aligns with, but does not overlap the left side of the sub-patch. Crack propagation causes the shorted unit to shift leftward above the U-shaped resonator, increasing the overlapped length between the U-shaped resonator and the sub-patch beneath the shorted unit. Consequently, the electric length of the combined resonator

Table 3
Basic Parameters Of The Circular Broadband Antenna.

Parameters	Value	Parameters	Value
W_3 / mm	30	L_4 / mm	55
W_4 / mm	3	L_5 / mm	0.3
W_5 / mm	13.5	L_6 / mm	5
W_6 / mm	0.7	L_7 / mm	10
W_7 / mm	3.6	L_8 / mm	16
R_1 / mm	13	L_9 / mm	0.9

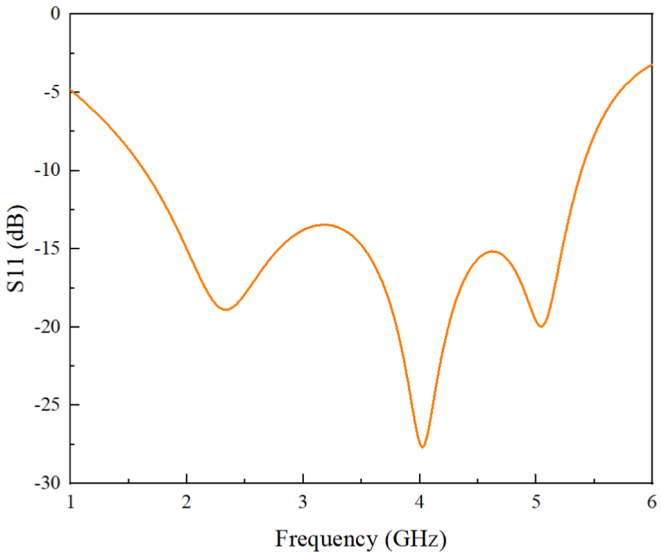

Fig. 14. Simulated reflection coefficient (S11) of the designed circular broadband antenna.

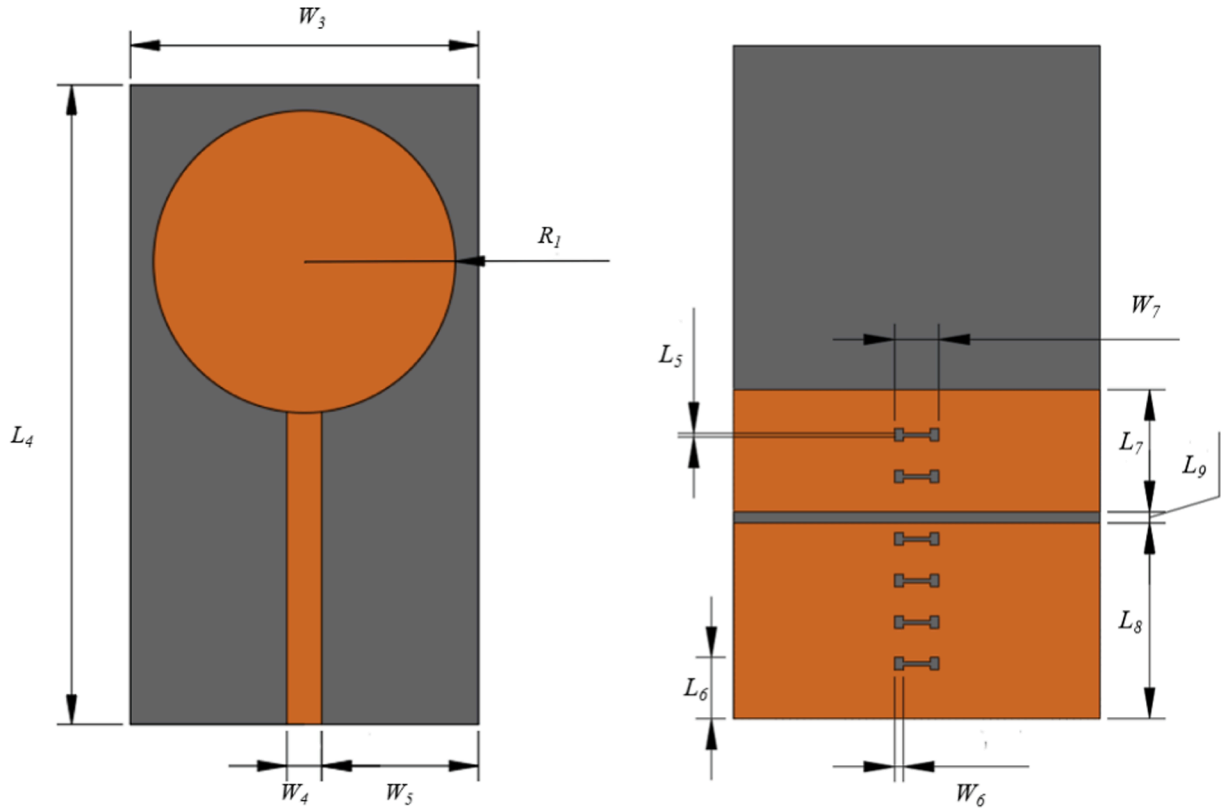

Fig. 13. Dimensional parameters of the circular broadband antenna: (a) Top view of sensing unit and (b) Upward view of the movable shorted unit.

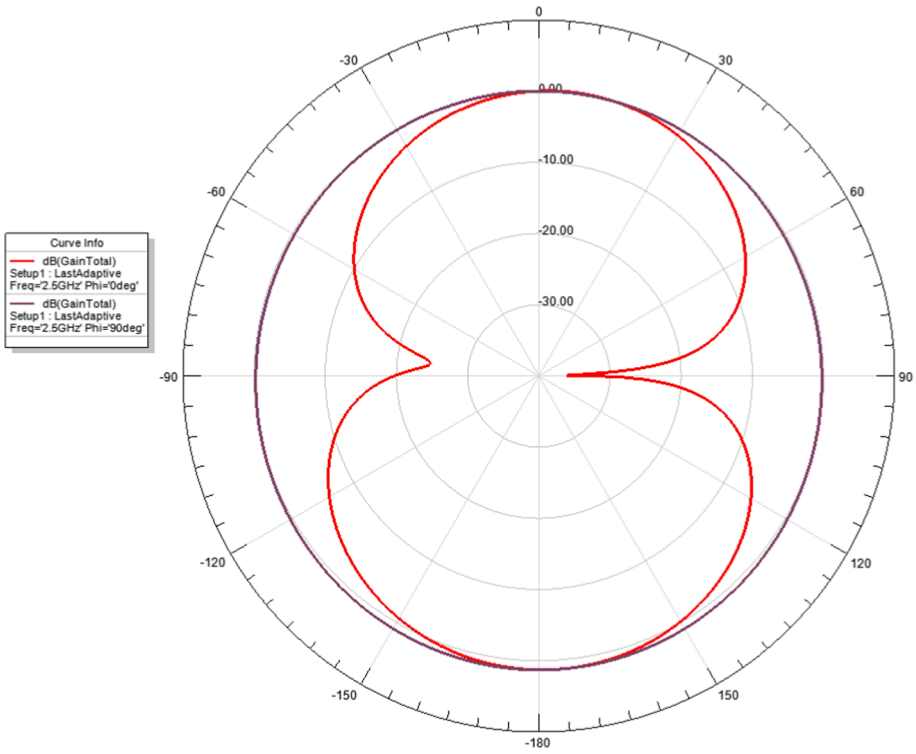

Fig. 15. E-plane and H-plane gain plot of the designed circular broadband antenna.

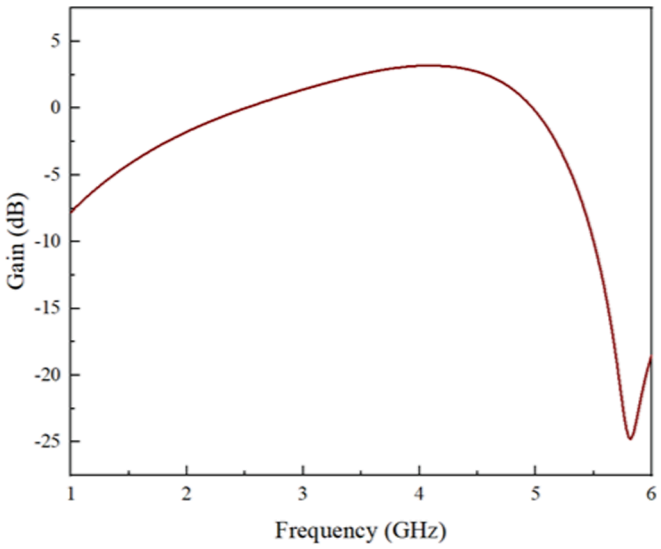

Fig. 16. Simulated gain plot of the designed circular broadband antenna.

decreases, leading to an increase in the resonant frequency of the combined resonator.

In order to realize wireless interrogation of antenna sensors, two UWB antennas need to be connected to two ports of the vector network analyzer (VNA), as shown in Fig. 4. The VNA inquiry signal is transmitted through Tx antenna 1, and when the sensor's Rx antenna 1 receives the signal, the Rx antenna 1 generates a surface current. This current flows to the sensor's Tx antenna 2 through the sensing element, which encodes deformation information in the current. Then Tx antenna 2 resonates to transmit the encoded signal to VNA's Rx antenna 2. From the insertion loss and transmission phase read by the VNA, the combined resonator's resonant frequency can be extracted, and then the crack width can be calculated.

Fig. 5 shows the dimensional parameters of the sensing unit. W and L are the width and length of the substrate, respectively. W_1 is the length of the vertical portion of the microstrip line and L_1 is the length of the horizontal portion of the microstrip line. g is the gap between the U-shaped resonator and the microstrip line. L_2 is the length of the horizontal portion of the U-shaped resonator, W_2 the length of the vertical portion of the U-shaped resonator, and s is the width of the U-shaped resonator. L_3 is the length of the sub-patch. ΔL *is* the overlapped length between the U-shaped resonator and the sub-patch.

In order to reveal the sensing principle of the sensor intuitively, the equivalent circuit model of the sensor is established, as shown in Fig. 6. The flanged microstrip line is equivalent to a parallel *RLC* network, and the combined resonator (U-shaped resonator and sub-patch) can also be modeled with a parallel *RLC* network. When the surface current flows through the microstrip line, there will be magnetic coupling L_m and electric coupling C_m between the combined resonator and the microstrip line [14], which causes the combined resonator to resonate at its resonant frequency and dissipate the energy of the interrogation signal at that frequency component. According to the equivalent circuit model, the resonant frequency of the combined resonator can be calculated as [40,41]:

$$f_c = \frac{1}{\sqrt{L_c C_c}} \tag{5}$$

Where L_c is the equivalent inductance of the combined resonator, and C_c is the equivalent capacitance of the combined resonator. The equivalent circuit parameters of the combined resonator can be determined by[40]:

$$C_c = \frac{\omega_c}{2Z_0(\omega_0^2 - \omega_c^2)} \tag{6}$$

$$L_c = \frac{\omega_c}{4\pi^2 f_0^2 C_c} \tag{7}$$

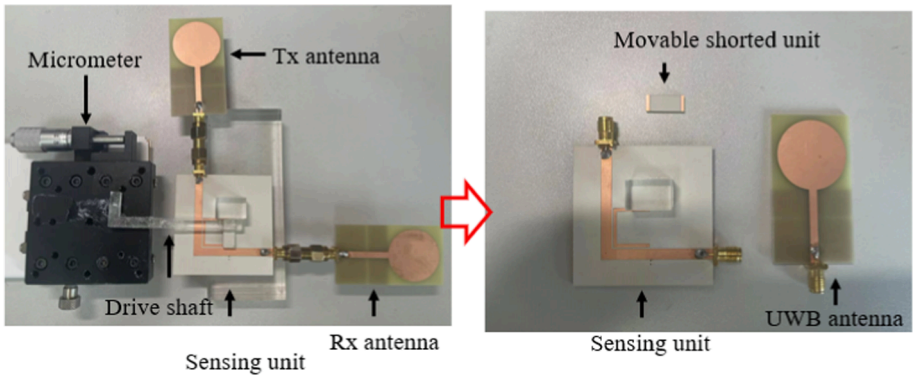

Fig. 17. The proposed crack sensor.

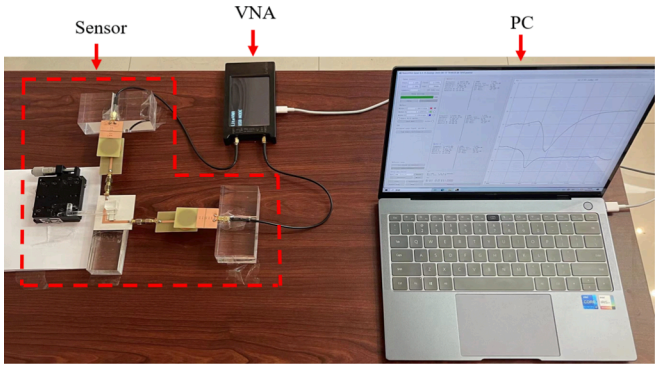

Fig. 18. Test system setup on wood for the VNA experiment.

$$R = \frac{2Z_0}{\sqrt{\frac{1}{(S_{11}(\omega_0))^2} - (2Z_0(\omega_0 C - \frac{1}{\omega_0 L_C}))^2 - 1}} \tag{8}$$

Where ω_0 is the angular resonance frequency, ω_c is the 3-dB cutoff angular frequency, and Z_0 is the characteristic impedance of the microstrip line.

Meanwhile, there is another, more convenient method for calculating the resonant frequency of a combined resonator which utilizes the concept of effective electrical length. The resonant frequency of the combined resonator can also be calculated as[41,42]:

$$f_c = \frac{c}{2L_e}\sqrt{\frac{2}{\varepsilon_r + 1}} \tag{9}$$

Where c is the speed of light in a vacuum, ε_r is the relative dielectric constant of the dielectric substrate, and L_e is the effective electrical length of the combined resonator and can be calculated as:

$$L_e = 2{\cdot}L_2 + W_2 + 2{\cdot}L_3 - 2{\cdot}\Delta L \tag{10}$$

When the movement of the shorted unit relative to the U-shaped resonator is very small, that is, the change of the combined resonator's effective electrical length (L_e) is small enough, the resonant frequency's shift and the change in L_e shows a linear relationship approximatively. As shown in the following equation:

$$f_c = -\frac{c}{2L_e^2}\sqrt{\frac{2}{\varepsilon_r + 1}}\triangle L \tag{11}$$

3. Simulation

3.1. Simulation of the sensing element in CST

To evaluate the detection performance of the proposed crack sensor, the sensor is simulated in CST Microwave Studio, as shown in Fig. 7. The model uses two wave ports for interrogating the sensing element and receiving retransmitted signals, respectively, avoiding the employment of cross-polarized Rx and Tx antennas, which simplifies the simulation process without compromising performance verification. The material of the dielectric substrate is Rogers RO3003. The microstrip line, ground plane, U-shaped resonator, and overlapping sub-patch are all set as perfect electric conductors (PECs).

The dimensions of the crack sensor are detailed in Table 1. In the model, the U-shaped resonator and the sub-patch are situated on the same plane, ensuring there is no air gap between them to facilitate the flow of current. To simulate the spread of the crack, the overlapped length between the U-shaped resonator and the sub-patch was set as a variable with a range of 0–2 mm and a change in step size of 0.2 mm. The entire simulation space is determined by the cube box in Fig. 7, filled with air, and the sensor is located in the center of the cube box. The sensor is fed by waveport 1, and the resultant signal is received by waveport 2 after it flows through the flanged microstrip line.

Initially, the right side of the U-shaped resonator fits but does not overlap the left side of the sub-patch. Subsequently, the spread of the crack will cause the sub-patch to move to the left, resulting in an overlapped length with the U-shaped resonator. This overlapped length leads to a reduction in the effective electrical length of the combined resonator. To investigate the correlation between the resonant frequency of the combined resonator and the overlapped length, a series of simulations are conducted, varying the overlapped length from 0 mm to 2 mm in increments of 0.2 mm to represent the step of crack expansion. Fig. 8 shows the insertion loss curve and transmission phase curve under different overlapped lengths. Then, the lowest point of each insertion loss curve and the initial point where the phase fluctuates are taken as resonance points, and the variation curve of resonance frequency and crack width are established, respectively, as shown in Fig. 9.

Obviously, with the expansion of the crack, the U-shaped resonator and the sub-patch gradually overlap, and then the resonant frequency of the combined resonantor increases correspondingly. The comparison of calculation results using insertion loss and transmission phase is presented in Table 2. Although there is a slight discrepancy in the resonant frequencies obtained through insertion loss and transmission phase, a specific frequency range can be defined to represent different crack propagation states in practical applications. There is a clear linear relationship between the resonant frequency and the overlapped length calculated by both methods, and the fitting factor of both curves is 0.9984, as shown in Fig. 7. The resonant frequency obtained by these two methods is approximately shifted about 129 MHz for every 1 mm crack propagation, indicating that the sensor has high sensitivity in monitoring crack width.

To further verify the detection mechanism of the sensor, Fig. 10 shows the current distribution on the antenna sensor at 2.6 GHz when the crack width extends to 1 mm. Clearly, the current predominantly

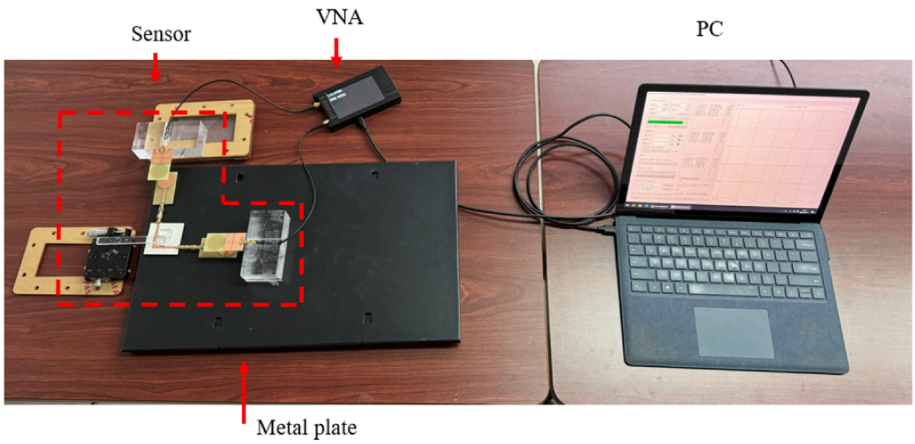

(a)

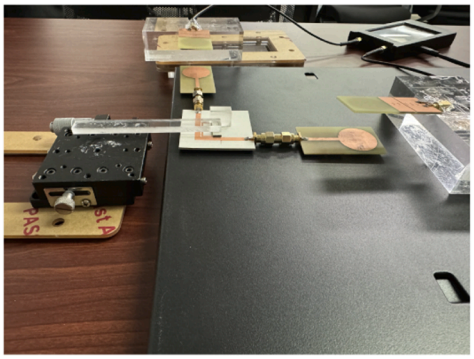

(b)

Fig. 19. Test system setup on a metal plate for the VNA experiment: (a) total system and (b) detail diagram of the sensor.

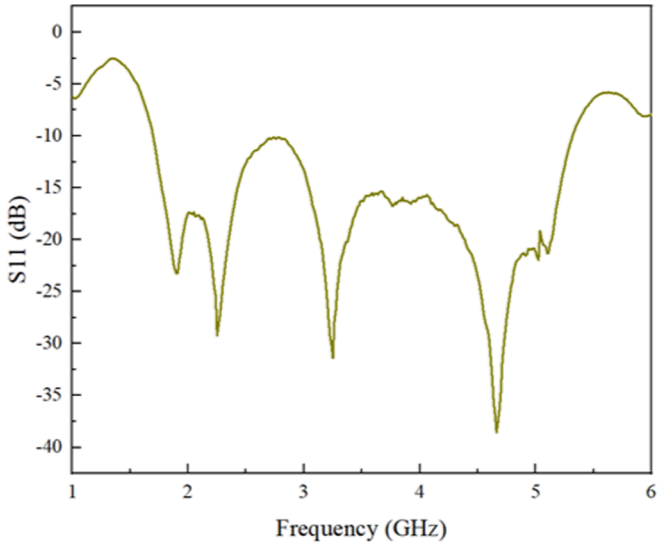

Fig. 20. Measured reflection coefficient (S11) of the designed circular broadband antenna.

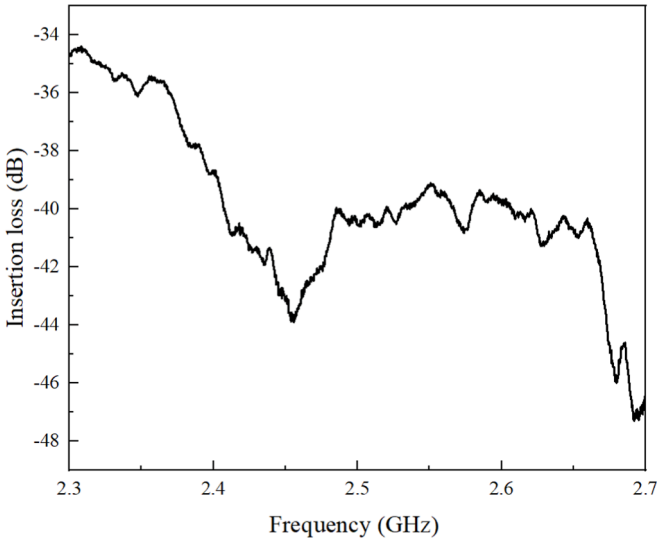

Fig. 21. Insertion loss in sensor-absent environments.

concentrates on both the U-shaped resonator and the sub-patch. Fig. 11 and Fig. 12 show the electric field distribution and magnetic field distribution of the crack sensor at 2.6 GHz when the crack width extends to 1 mm, respectively. The electric field and magnetic field are strongest near the combined resonator, indicating that the combined resonator has resonated. This observation aligns with the theoretical analysis presented in the preceding section.

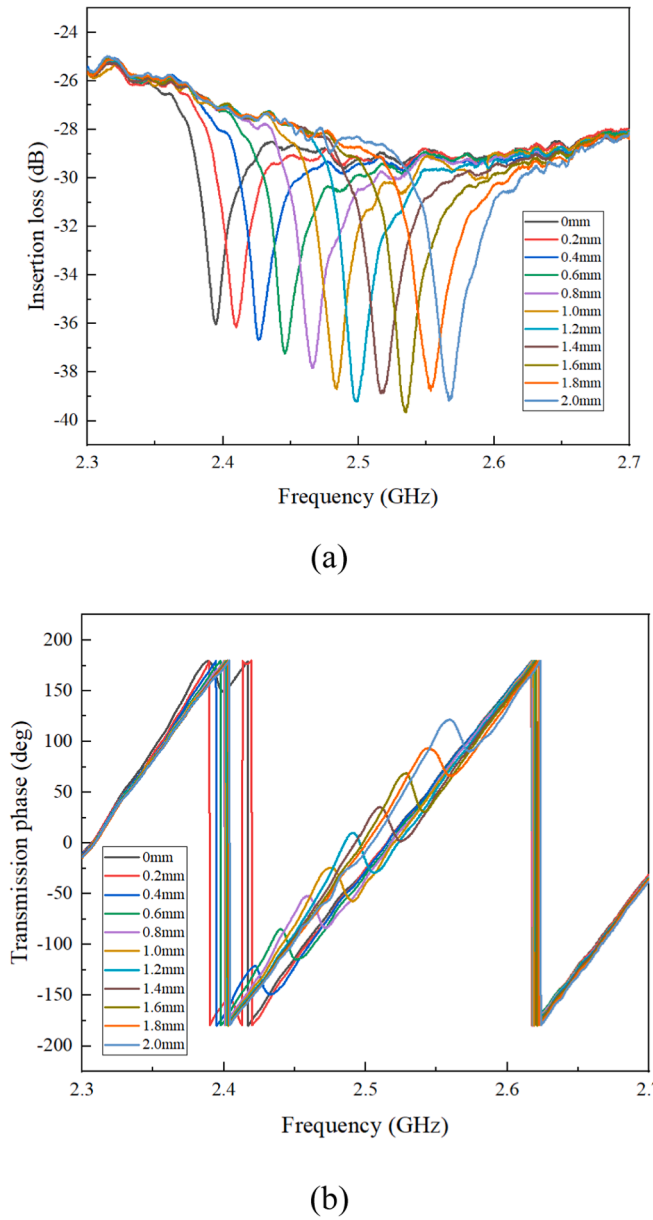

Fig. 22. S21 curve of the crack sensor mounted on wood under different overlapped lengths: (a) insertion loss and (b) transmission phase.

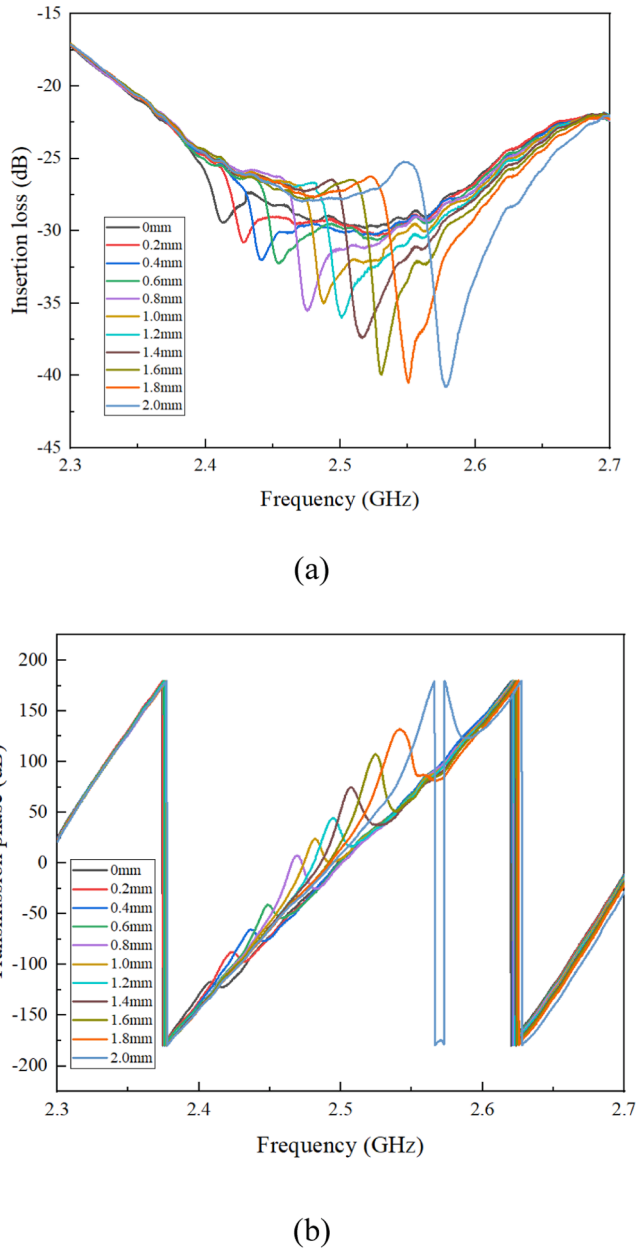

Fig. 23. S21 curve of the crack sensor mounted on metal plates under different overlapped lengths: (a) insertion loss and (b) transmission phase.

3.2. Simulation of the UWB antenna in HFSS

As discussed earlier, the sensor needs to integrate two UWB antennas at both ends of the sensing element to receive the inquiry signal and retransmit the signal encoded with the deformation information. To meet the requirement of the sensing element's operating frequency band, the circular broadband antenna is designed and simulated in Ansys high-frequency structure simulator (HFSS) [43]. Fig. 13 and Table 3 show the circular broadband antenna parameters and dimensions. The material of the dielectric substrate is FR4, and the thickness of the substrate is 1.6 mm.

The reflection coefficient and the antenna radiation patterns of the circular wideband antenna are shown in Fig. 14 and Fig. 15, respectively. Obviously, the simulated bandwidth of the proposed antenna is 1.64——5.38 GHz. Fig. 16 shows the simulated gain of the proposed antenna. Limited by the substrate material and the size of the patch antenna, the maximum gain of the antenna is 1.30 in the 2——3 GHz. The calculated boundary between the near field and the far field of the circular wideband antenna is 1.1 cm.

4. Wireless interrogation

In this section, the antenna sensor is fabricated, and a series of experiments are carried out to validate the sensor's operational performance and feasibility.

The physical image of the sensor is shown in Fig. 17, and its substrate material and specific size parameters are consistent with the simulation model. The crack sensor is interrogated wirelessly on wood and metal surfaces by VNA and UWB antennas, respectively, as shown in Fig. 18 and Fig. 19. The dielectric constant of wood is 1.5 ~ 3.5, and the dielectric constant of metals is infinite. The width of the cracks is increased from 0 mm to 2 mm, and the step size is 0.2 mm. The two ports of the VNA are connected to the UWB antenna through the coaxial line, with one port responsible for transmitting the interrogation signal and the other for receiving retransmission signals. Simultaneously, the

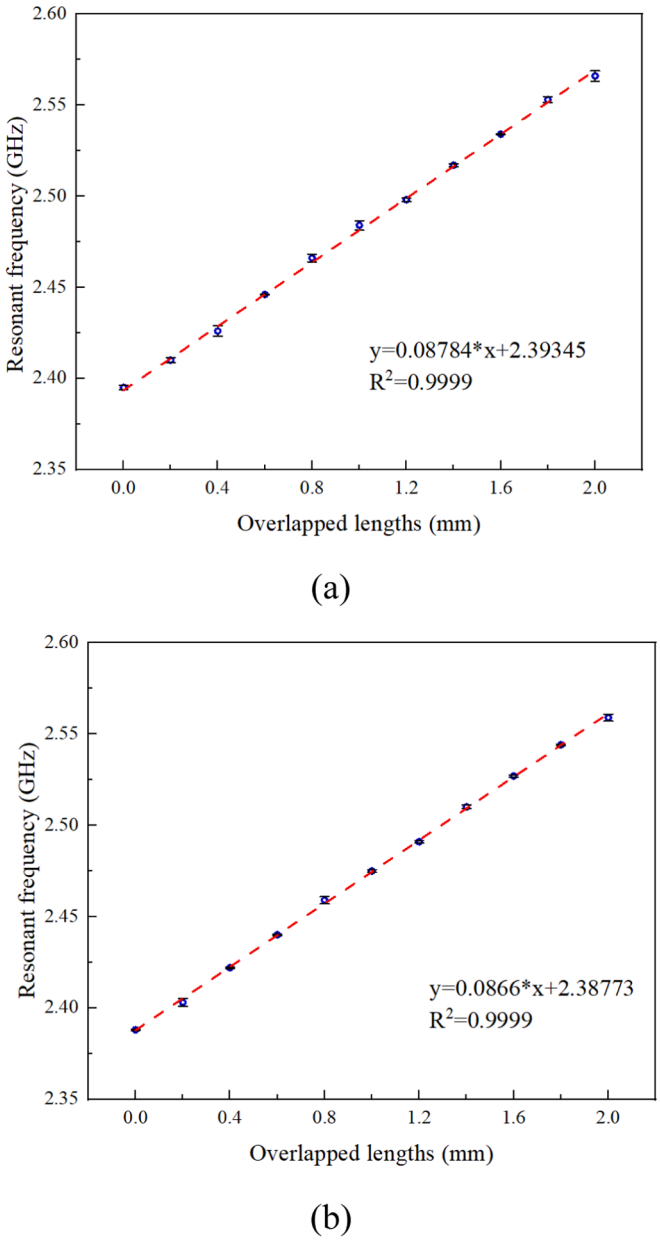

Fig. 24. Relationship between overlapped lengths and resonant frequency calculated from (a)insertion loss and (b) transmission phase (sensor is mounted on wood).

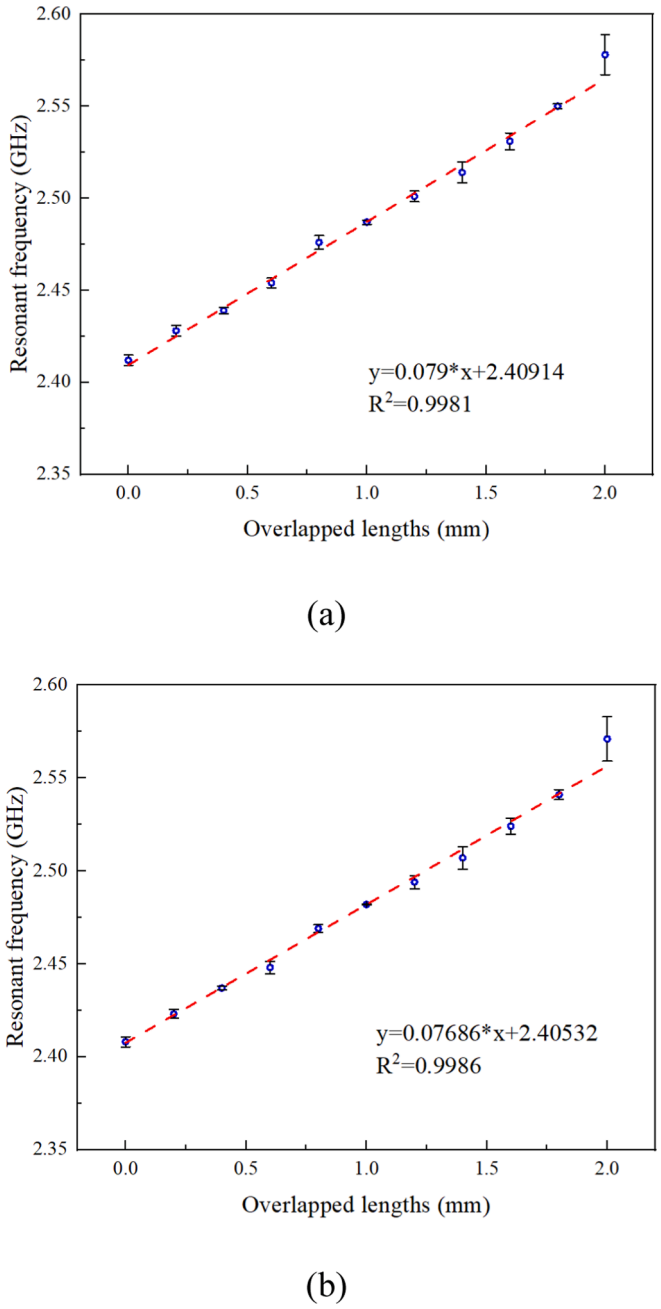

Fig. 25. Relationship between overlapped lengths and resonant frequency calculated from (a) insertion loss and (b) transmission phase (sensor is mounted on metal plates).

antenna sensor is connected to another pair of UWB antennas, which are responsible for receiving the interrogation signal from the VNA and transmitting the antenna sensor's encoded signal. Furthermore, the Tx and Rx antennas are configured with cross polarization to avoid unwanted environment reflected signal.

As shown in Fig. 17 and Fig. 19(b), the movable shorted unit is connected to the micrometer through a transparent acrylic plate. The micrometer facilitates precise control over the displacement of the movable table, subsequently driving the movement of the shorted unit through the drive shaft to simulate crack propagation. Initially, the right side of the U-shaped resonator aligns without overlapping the left side of the sub-patch. Then, by manipulating the micrometer, the movable shorted unit is controlled to move toward the U-shaped resonator, so that the sub-patch overlaps partially with the U-shaped resonator. The incremental movement of the shorted unit is set at 0.2 mm. The measured reflection coefficient of the circular wideband antenna is shown in Fig. 20, and the bandwidth of the proposed antenna is 1.70——5.31 GHz. Fig. 21 records the insertion loss curve in an empty environment where no sensor is installed. Obviously, the signal strength is lower than −35 dB, indicating excellent cross polarization performance. The insertion loss and transmission phase of the antenna sensor mounted on wood and metal plates under different overlapped lengths are recorded by vector network analyzer (VNA), as shown in Fig. 22 and Fig. 23, respectively. When the sensor is placed above wood, the maximum wireless reading distance is 7 cm, and when the sensor is placed above metal, the maximum wireless reading distance is 6 cm. The key factors that limit the reading distance are the signal power of the VNA is only 0 dBm and the gain of the UWB antenna is not high enough.

The sensor's resonant frequencys are derived from the lowest point of each insertion loss curve and the initial point of phase fluctuation of each transmission phase curve, respectively. The relationship between

Table 4
Comparison of theoretical calculation, simulation, and VNA experiment.

Calculation basis	Theoretical calculation Equivalent electrical length	CST simulation Amplitude	Phase	VNA experiment (on wood) Amplitude	Phase	VNA experiment (on metal plates) Amplitude	Phase
Measuring range (GHz)	2.411–2.652	2.480-2.738	2.473-2.732	2.395–2.566	2.388–2.559	2.412–2.578	2.408–2.571
Fitting factor	–	0.9984	0.9984	0.9999	0.9999	0.9981	0.9986
Sensitivity (MHz/mm)	120.5	129	129.5	85.5	85.5	83	81.5

Table 5
Comparison of similar work and this work.

Ref.	Application	Wireless reading technology	Sensing variable	Stress state	Sensitivity
[44]	Strain detection	Co-polarization	Amplitude	Stressed	32.77 MHz/%ε
[45]	Crack detection	Co-polarization	Amplitude	Unstressed	68 MHz/mm
[46]	Crack detection	Co-polarization	Amplitude	Unstressed	43.9 MHz/mm
[40]	Strain detection	Cross polarization	Amplitude	Stressed	1.90909 KHz/με
[22]	Crack detection	Co-polarization	Amplitude	Unstressed	66.7 MHz/mm
This work	Crack detection	Cross polarization	Amplitude and phase	Unstressed	85.5 MHz/mm

overlapped lengths and resonant frequency are displayed in Fig. 24 and Fig. 25. Apparently, the resonance frequency increases linearly with the expansion of the crack. Both the linear fitting coefficients are higher than 0.99, demonstrating the excellent workability of the crack sensor.

Table 4 provides a comparison between theoretical calculation, simulation results, and VNA experiment results. The correlation coefficients for the fitted line in each group are higher than 0.99, revealing the outstanding functionality of the antenna sensor. Although the resonant frequencies calculated by amplitude and phase are slightly different, a certain frequency range can be defined to represent various crack propagation states in practical applications.

The main reasons for the disparities between the experimental and simulated results are: (a) a distinct air gap exists between the U-shaped resonator and the sub-patch in the experiments, whereas no such gap is considered in the simulation; (b) inherent size errors may occur during the manufacturing process of the antenna sensor; and (c) during manual control of the sub-patch's movement towards the U-shaped resonator, slight translations or rotations away from the intended displacement direction are inevitable, influencing the electromagnetic characteristics of the antenna sensor.

Table 5 provides a comparison between this work and similar work, which utilize RFID sensors to detect deformation. It is clear from the comparison table that the proposed sensor is more suitable for crack detection.

5. Conclusion

This paper introduced a novel cross-polarized antenna sensor based on a U-shaped resonator for stable and precise wireless passive crack sensing. The primary purpose of the sensor is to characterize the crack expansion by the relative displacement between the U-shaped resonator and the shorted unit, avoiding the force of the sensor itself, and employ cross polarization technique in wireless interrogation, avoiding signal's self-jamming. Meanwhile, the sensing element encodes the crack width information in the amplitude and phase of the retransmission signal, and the resonant frequency can be extracted from both the amplitude and phase, enhancing the stability and accuracy in the wireless sensing. The wireless channel model of the sensing system is established to reveal the mechanism of cross polarization technique to avoid self-jamming. Furthermore, the equivalent circuit model of the antenna sensor is established to verify its effectiveness. Both the results of the simulation and experiment show that the sensor has excellent working performance. The sensor's resonant frequency is linear with the crack width, and the correlation coefficient exceeds 0.99.

In the future, the authors will involve exploring the utilization of Unmanned Aerial Vehicles (UAVs) equipped with UWB antennas and VNA to retrieve data from the sensor in real-world environments.

CRediT authorship contribution statement

Kang Jiang: Writing – original draft, Software, Formal analysis, Conceptualization. **Songtao Xue:** Writing – review & editing, Supervision, Data curation, Conceptualization. **Liyu Xie:** Writing – review & editing, Validation, Methodology, Conceptualization. **Guochun Wan:** Writing – review & editing, Project administration, Methodology, Investigation, Data curation.

Declaration of competing interest

The authors declare that they have no known competing financial interests or personal relationships that could have appeared to influence the work reported in this paper.

Data availability

Data will be made available on request.

Anowledgements

This research was funded by the National Natural Science Foundation of China (Grant No. 52178298, 52078375, and 52378311).

References

[1] C. Scuro, F. Lamonaca, S. Porzio, G. Milani, R. Olivito, Internet of Things (IoT) for masonry structural health monitoring (SHM): Overview and examples of innovative systems, Construction and Building Materials 290 (2021) 123092.
[2] T.-H. Lin, A. Putranto, Y.-T. Wang, Smart sensor tags for seepage sensing protected by 3D-printed case for embedding in concrete structures, Construction and Building Materials 284 (2021) 122784.
[3] A.K. Jha, A. Lamecki, M. Mrozowski, M. Bozzi, A microwave sensor with operating band selection to detect rotation and proximity in the rapid prototyping industry, IEEE Transactions on Industrial Electronics 68 (2020) 683–693.
[4] J. Wang, Y. Han, Z. Cao, X. Xu, J. Zhang, F. Xiao, Applications of optical fiber sensor in pavement Engineering: A review, Construction and Building Materials 400 (2023) 132713.
[5] W. Qian, C. Qian, Long-Range Detection of a Wirelessly Powered Resistive Transducer, IEEE Transactions on Instrumentation and Measurement 71 (2022) 1–9.
[6] X. Qing, W. Li, Y. Wang, H. Sun, Piezoelectric transducer-based structural health monitoring for aircraft applications, Sensors 19 (2019) 545.
[7] A.D. Eslamlou, A. Ghaderiaram, E. Schlangen, M. Fotouhi, A review on non-destructive evaluation of construction materials and structures using magnetic sensors, Construction and Building Materials 397 (2023) 132460.
[8] S.M. Khan, N. Qaiser, S.F. Shaikh, M.M. Hussain, Design analysis and human tests of foil-based wheezing monitoring system for asthma detection, IEEE Transactions on Electron Devices 67 (2019) 249–257.

[9] M. Gao, P. Wang, Y. Wang, L. Yao, Self-powered ZigBee wireless sensor nodes for railway condition monitoring, IEEE Transactions on Intelligent Transportation Systems 19 (2017) 900–909.
[10] S. Dey, R. Bhattacharyya, S.E. Sarma, N.C. Karmakar, A. Novel, Smart Skin, Sensor for Chipless RFID-Based Structural Health Monitoring Applications, IEEE Internet of Things Journal 8 (2020) 3955–3971.
[11] K. Jiang, L. Xie, S. Xue, G. Wan, Capacitively-coupled dual ring antennas for bolt loosening detection, Measurement 200 (2022) 111605.
[12] S.K. Behera, Chipless RFID sensors for wearable applications: A review, IEEE Sensors Journal 22 (2021) 1105–1120.
[13] H. Huang, Flexible wireless antenna sensor: A review, IEEE Sensors Journal 13 (2013) 3865–3872.
[14] S. Deif, M. Daneshmand, Multiresonant chipless RFID array system for coating defect detection and corrosion prediction, IEEE Transactions on Industrial Electronics 67 (2019) 8868–8877.
[15] Z.R. Yi, S.T. Xue, L.Y. Xie, G.C. Wan, Detection of setting time in cement hydration using patch antenna sensor, STRUCTURAL CONTROL & HEALTH MONITORING 29 (2022).
[16] F.M. Tchafa, H. Huang, Microstrip patch antenna for simultaneous temperature sensing and superstrate characterization, Smart Materials and Structures 28 (2019) 105009.
[17] A.M.J. Marindra, G.Y. Tian, Multiresonance chipless RFID sensor tag for metal defect characterization using principal component analysis, IEEE Sensors Journal 19 (2019) 8037–8046.
[18] J.W. Sanders, J. Yao, H. Huang, Microstrip Patch Antenna Temperature Sensor, IEEE Sensors Journal 15 (2015) 5312–5319.
[19] X. Yi, C. Cho, J. Cooper, Y. Wang, M.M. Tentzeris, R.T. Leon, Passive wireless antenna sensor for strain and crack sensing—Electromagnetic modeling, simulation, and testing, Smart Materials and Structures 22 (2013) 085009.
[20] C. Cho, X. Yi, D. Li, Y. Wang, M.M. Tentzeris, Passive wireless frequency doubling antenna sensor for strain and crack sensing, IEEE Sensors Journal 16 (2016) 5725–5733.
[21] A. Lazaro, R. Villarino, F. Costa, S. Genovesi, A. Gentile, L. Buoncristiani, D. Girbau, Chipless dielectric constant sensor for structural health testing, IEEE Sensors Journal 18 (2018) 5576–5585.
[22] A.M.J. Marindra, G.Y. Tian, Chipless RFID sensor tag for metal crack detection and characterization, IEEE Transactions on Microwave Theory and Techniques 66 (2018) 2452–2462.
[23] Z. Yi, S. Xue, L. Xie, G. Wan, C. Wan, A Slotted-Patch Antenna Sensor With Higher Sensitivity for Detecting Setting Time of Cement Paste, IEEE Transactions on Instrumentation and Measurement 71 (2022) 1–13.
[24] X. Li, S. Xue, L. Xie, G. Wan, A miniaturized passive wireless patch antenna sensor for structural crack sensing, Structural Health Monitoring (2024) 14759217241227797.
[25] S.T. Xue, K.Q. Xu, L.Y. Xie, G.C. Wan, Crack sensor based on patch antenna fed by capacitive microstrip lines, SMART MATERIALS AND STRUCTURES 28 (2019).
[26] S. Xue, Z. Zheng, S. Guan, L. Xie, C.J.S. Wan, A Capacitively-Fed Inverted-F Antenna for Displacement Detection in Structural Health Monitoring 20 (2020).
[27] S.T. Xue, Z.R. Yi, L.Y. Xie, G.C. Wan, T. Ding, A Displacement Sensor Based on a Normal Mode Helical Antenna, SENSORS 19 (2019).
[28] S.T. Xue, K. Jiang, S. Guan, L.Y. Xie, G.C. Wan, C.F. Wan, Long-Range Displacement Meters Based on Chipped Circular Patch Antenna, SENSORS 20 (2020).
[29] S Xue, H. Wang, L Xie, G. Wan, Bolt loosening detection method based on double-layer slotted circular patch antenna, Structural Health Monitoring (2024) 14759217241227992.
[30] J. Zhang, B. Huang, G. Zhang, G.Y. Tian, Wireless passive ultra high frequency RFID antenna sensor for surface crack monitoring and quantitative analysis, Sensors 18 (2018) 2130.
[31] S. Caizzone, E. DiGiampaolo, Wireless Passive RFID Crack Width Sensor for Structural Health Monitoring, IEEE SENSORS JOURNAL 15 (2015) 6767–6774.
[32] S. Xue, X. Li, L. Xie, Z. Yi, G. Wan, A bolt loosening detection method based on patch antenna with overlapping sub-patch, Structural Health Monitoring 21 (2022) 2231–2243.
[33] S. Deshmukh, H. Huang, Wireless interrogation of passive antenna sensors, MEASUREMENT SCIENCE AND TECHNOLOGY 21 (2010).
[34] X. Xu, H. Huang, Battery-less wireless interrogation of microstrip patch antenna for strain sensing, SMART MATERIALS AND STRUCTURES 21 (2012).
[35] F. Babaeian, N.C. Karmakar, Time and frequency domains analysis of chipless RFID back-scattered tag reflection, IoT 1 (2020) 109–127.
[36] A.M.J. Marindra, G.Y. Tian, Chipless RFID sensor for corrosion characterization based on frequency selective surface and feature fusion, Smart Materials and Structures 29 (2020) 125010.
[37] R. Khalifeh, M.S. Yasri, B. Lescop, F. Gallée, E. Diler, D. Thierry, S. Rioual, Development of wireless and passive corrosion sensors for material degradation monitoring in coastal zones and immersed environment, IEEE Journal of Oceanic Engineering 41 (2016) 776–782.
[38] A. Vena, E. Perret, S. Tedjni, A depolarizing chipless RFID tag for robust detection and its FCC compliant UWB reading system, IEEE Transactions on Microwave Theory and Techniques 61 (2013) 2982–2994.
[39] S. Preradovic, N.C. Karmakar, Design of chipless RFID tag for operation on flexible laminates, IEEE Antennas and Wireless Propagation Letters 9 (2010) 207–210.
[40] L. Chen, L. Liu, L. Kang, Z. Wan, G. Wan, L. Xie, A Multibranch U-Shaped Tunable Encoding Chipless RFID Strain Sensor for IoT Sensing System, IEEE Internet of Things Journal 10 (2022) 5304–5320.
[41] Z. Wang, Z. Zhang, Y. Hu, H. Zhang, X. Wang, Design of a novel compact and flexible chipless RFID tag based on an improved U-shaped resonator, Journal of Electromagnetic Waves and Applications 36 (2022) 1672–1684.
[42] M.A. Islam, N.C. Karmakar, Real-world implementation challenges of a novel dual-polarized compact printable chipless RFID tag, IEEE Transactions on Microwave Theory and Techniques 63 (2015) 4581–4591.
[43] D. Gopi, A.R. Vadaboyina, J.K. Dabbakuti, DGS based monopole circular-shaped patch antenna for UWB applications, SN Applied Sciences 3 (2021) 198.
[44] K. Mc Gee, P. Anandarajah, D. Collins, Proof of concept novel configurable chipless RFID strain sensor, Sensors 21 (2021) 6224.
[45] S.T. Xue, Z.R. Yi, L.Y. Xie, G.C. Wan, Double-frequency passive deformation sensor based on two-layer patch antenna, SMART STRUCTURES AND SYSTEMS 27 (2021) 969–982.
[46] X. Li, S. Xue, L. Xie, G. Wan, C. Wan, An off-center fed patch antenna with overlapping sub-patch for simultaneous crack and temperature sensing, Smart Materials and Structures 31 (2022) 095036.